J. Fluid Mech. (2018), *vol.* 848, *pp.* 946–967.
doi:10.1017/jfm.2018.359

Unsteady sheet fragmentation: droplet sizes and speeds

Y. Wang[1] **and L. Bourouiba**[1,†]

[1]The Fluid Dynamics of Disease Transmission Laboratory, Massachusetts Institute of Technology, Cambridge, MA 02139, USA

(Received 3 January 2018; revised 22 March 2018; accepted 23 April 2018)

Understanding what shapes the drop size distributions produced from fluid fragmentation is important for a range of industrial, natural and health processes. Gilet & Bourouiba (*J. R. Soc. Interface*, vol. 12, 2015, 20141092) showed that both the size and speed of fragmented droplets are critical to transmission of pathogens in the agricultural context. In this paper, we study both the size and speed distributions of droplets ejected during a canonical unsteady sheet fragmentation from drop impact on a target of comparable size to that of the drop. Upon impact, the drop transforms into a sheet which expands in the air bounded by a rim on which ligaments grow, continuously shedding droplets. We developed high-precision tracking algorithms that capture all ejected droplets, measuring their size and speed, as well as the detachment time from, and link to, their ligament of origin. Both size and speed distributions of all ejected droplets are skewed. We show that the polydispersity and skewness of the distributions are inherently due to the unsteadiness of the sheet expansion. We show that each ligament sheds a single drop at a time throughout the entire sheet expansion by a mechanism of end-pinching. The droplet-to-ligament size ratio $R \approx 1.5$ remains constant throughout the unsteady fragmentation, and is robust to change in impact Weber number. We also show that the population mean speed of the fragmented droplets at a given time is equal to the population mean speed of ligaments one necking time prior to detachment time.

Key words: aerosols/atomization, drops, instability

1. Introduction

Fluid fragmentation has been studied in a range of contexts (Villermaux 2007; Josserand & Thoroddsen 2016) with a main focus on understanding the size distribution of secondary droplets, due to their importance for a wide range of applications in industrial processes, such as spray coating, cleaning, agricultural irrigation, fuel combustion and heat transfer (Yarin 2006). Fluid fragmentation also plays an important role in pathogen transmission (Bourouiba, Dehandschoewercker & Bush 2014; Gilet & Bourouiba 2014, 2015; Scharfman *et al.* 2016). Both the sizes and speeds of the produced droplets are critical in shaping the range and severity of contamination.

† Email address for correspondence: lbouro@mit.edu

Prior studies focused on the measurement of mean drop sizes produced as a function of the fragmentation process involved and parameters such as the speed and fluid properties of the impacting liquid jet or drop involved, nozzle geometry or surface properties, with the goal of control and optimization of spray drop sizes. Typically, measured drop size distributions are fitted by exponential, Poisson, log-normal or families of gamma distributions all capturing various degrees of polydispersity common in the final drop size distributions measured. Some of the distributions fitted are rooted in relevant physical interpretations of the mechanism of fluid fragmentation while others are not (Villermaux 2007). In practice, at least one free parameter is used in such fits and different functional forms of distributions can be made to match the same experimental data, even when the physical processes underlying the distribution model used for the fit are contradictory. Picking the wrong model fit leads to misunderstanding of the underlying physics and hinders optimized control of sprays and technological advances with important industrial, environmental and health implications. Physical insights on the detailed construction of drop size distributions focused mainly on steady or stationary fragmentation, where droplet properties are considered independent of time (Clanet & Villermaux 2002), or instantaneous fragmentation, where all droplets are expected to be created simultaneously. However, an important class of fragmentation processes in nature and industry are in fact unsteady, continuously generating droplets of properties that vary with time.

Compared to a relatively rich literature proposing a range of families and mechanisms that select drop size distributions (Villermaux 2007), droplet speed distributions are seldom discussed. Thoroddsen, Takehara & Etoh (2012) studied the size and speed of micro-splashed droplets ejected at very early time $t \ll \tau_{imp}$ of unsteady sheet expansion from drop impact on solid surfaces. Here, $\tau_{imp} = d_0/u_0$ is the impact time scale and u_0 and d_0 are the velocity and diameter of the impacting drop, respectively. They showed that the size and ejection speed of droplets evolve with time. Riboux & Gordillo (2015) developed a model to rationalize and predict the speed of droplets generated in the early time of splash $t \ll \tau_{imp}$. However, most droplets are ejected during the entirety of a fragmentation process not just at the very early time. This is also the case for crown splash upon drop impact on a thin film, or crescent-moon splash from drop-on-drop collisions (Gilet & Bourouiba 2015; Wang & Bourouiba 2018). The droplet speed distribution of most fragmentation processes remains unknown.

Here, we focus on a canonical unsteady fragmentation process occurring upon drop impact on a small target of comparable size to that of the impacting drop (figure 1). This fundamental framework enables us to gain insights into the selection of ubiquitous polydispersed droplet size and speed distributions from unsteady fragmentation, which can be generalized and translated to a wide range of applications. We conducted systematic experiments and developed droplet and ligament detection, tracking and connection algorithms that capture all ejected droplets during rim fragmentation and link them to their ligaments of origin. The experiments and algorithms are described in § 2. These algorithms allowed us to discover three ejection modes of droplets during unsteady sheet fragmentation, which are discussed in § 3. We discuss the size distribution of ejected droplets in § 4 and show that their cumulative size distribution over time is shaped by the time evolution of their instantaneous population mean size, which we also show to be fully determined by their ligament of origin. The analogous discussion of the cumulative versus instantaneous droplet speed distributions is in § 5.

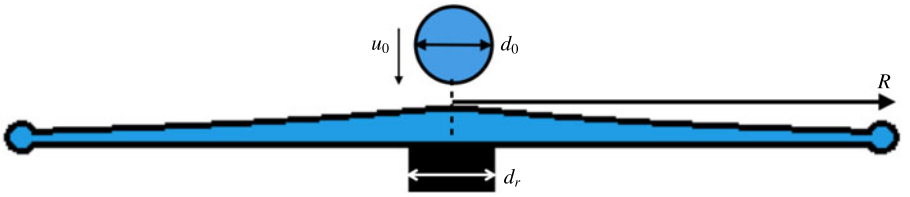

FIGURE 1. (Colour online) Schematic diagram of drop impact on a small surface of comparable size to that of the impacting drop, transformed into a horizontal expanding sheet. The optimal rod-to-drop diameter ratio used in the experiments is $\eta = d_r/d_0 = 1.44$ (Wang & Bourouiba 2017).

d_0 (mm)	u_0 (m s^{-1})	We	Re ($\times 10^4$)	N_{exp}	N_{drop}
	2.86 ± 0.01	494 ± 9	1.24 ± 0.02	30	134
4.33 ± 0.05	3.39 ± 0.01	693 ± 11	1.47 ± 0.02	30	167
	4.00 ± 0.01	967 ± 17	1.73 ± 0.03	30	234

TABLE 1. Experimental conditions used from impacting drop diameter d_0, impacting velocity u_0, to associated $We = \rho u_0^2 d_0/\sigma$ and $Re = u_0 d_0/\nu$, where $\rho = 1.0 \times 10^3$ kg m^{-3}, $\nu = 1.0 \times 10^{-6}$ m^2 s^{-1} and $\sigma = 72$ mN m^{-1}, are the density, kinematic viscosity and surface tension of the impacting drop, respectively. N_{exp} is the number of experiments carried for each Weber number and N_{drop} the average number of secondary droplets ejected for each experiment.

2. Observations and droplet–ligament connection algorithm

We conducted systematic experiments of canonical unsteady sheet fragmentation by impacting a drop on a cylindrical rod of comparable size to that of the drop. An impacting drop of diameter $d_0 = 4.33 \pm 0.05$ mm is released by a needle from three different heights. Drops are made of water and nigrosin dye at concentration 1.2 g l^{-1}, with density $\rho = 1.0 \times 10^3$ kg m^{-3}, surface tension $\sigma = 72$ mN m^{-1} and kinematic viscosity $\nu = 1.0 \times 10^{-6}$ m^2 s^{-1}. The rod is made of stainless steel with smooth top surface with contact angle between 52° and 81°. The diameter of the rod is 6.25 mm with a rod-to-drop size ratio of 1.44, which allows for a horizontal sheet expansion and negligible surface viscous dissipation (Wang & Bourouiba 2017). We use high-speed cameras to record the entire fragmentation process from both top and side views simultaneously. A monochrome high-speed camera is used to record the impacts from the top at 20 000 frame per second (fps) and with 768×768 pixel resolution. A colour camera is positioned on the side to record at 5000 fps and with 1280×1000 pixel resolution. The impact velocity of the drops for each experiment is directly measured from the side camera. The detailed experimental conditions and their associated Weber number, $We = \rho u_0^2 d_0/\sigma$, and Reynolds number, $Re = u_0 d_0/\nu$, are summarized in table 1.

Conventionally (Fantini, Tognotti & Tonazzini 1990; Yarin & Weiss 1995; Villermaux & Bossa 2011; Thoroddsen *et al.* 2012; Peters, van der Meer & Gordillo 2013), drop size distributions were obtained by measuring the diameter of all the droplets seen in a single image at the end of a fragmentation event or using a sequence of images with fixed temporal intervals spanning the duration of the fragmentation. On each image, droplet contours are detected and their diameter

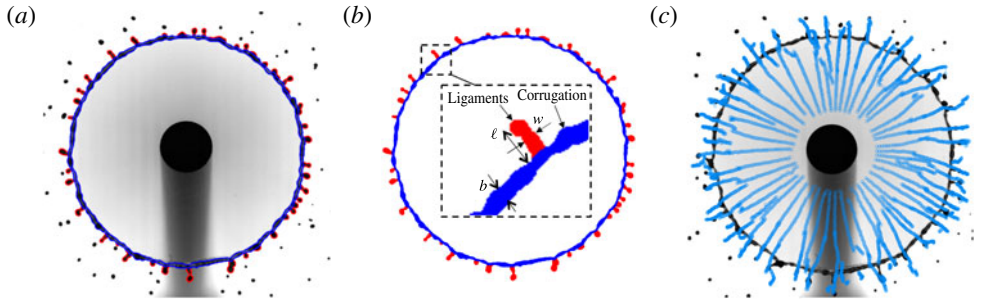

FIGURE 2. (Colour online) (*a*) Sheet fragmentation and (*b*) separation of the rim and ligament based on the inner and outer contours of the sheet detected by our algorithm. The inset shows a local rim–ligament structure, defining the ligament length l, its width w and rim thickness b. (*c*) Trajectories of the tip of all ligaments growing from the rim during the entire sheet expansion.

is inferred from the detected enclosed area. Such approaches are accurate for either droplets ejected continuously in steady fragmentation, such as a stationary Savart sheet (Savart 1833*a*,*b*; Clanet & Villermaux 2002), or for droplets ejected simultaneously, such as at the final breakup stage of an expanding sheet upon drop impact on a rod (Villermaux & Bossa 2011). For continuous droplet ejection throughout unsteady sheet fragmentation, a single image cannot capture the size and speed of all droplets ejected. When using sequences of frames (Yarin & Weiss 1995), if the time difference between two consecutive frames is too large, rapidly moving drops are missed. If the time difference is too small, double counting of slow droplets occurs. Both artefacts can lead to distortion of the final droplet size distribution produced. Moreover, the ejection time of each droplet, critical to quantifying unsteady fragmentation, is also missed by such approaches.

To guarantee accuracy in the capture of each ejected droplet without missing or double-counting sub-samples, we developed a ligament–droplet connection algorithm linking each ejected droplet to the ligament from which it detaches. The algorithm first captures the outline of each ligament at each time, and tracks its shape and location over time. Figure 2(*a*) illustrates the capture of both inner and outer contours of the rim–ligament system by our algorithm. We track local protrusions considered as ligaments when their length ℓ becomes larger than the local, instantaneous rim thickness b (figure 2*b*). The tracks in figure 2(*c*) show the trajectories of ligament tips throughout the sheet expansion. Droplets are continuously shed via ligament breakup. When a new droplet is shed, its ligament of origin suddenly shrinks. Thus, at each time, we consider new ejected droplets as those in the vicinity of a ligament that suddenly shrank. Based on this principle, our algorithm captures all droplets and identifies their ligament of origin, and precise detachment time.

Upon its ejection from a ligament, we can determine the size, speed and trajectory of a droplet. We developed a droplet-tracking algorithm specifically tailored to handle a wide range of droplet sizes and speeds. The algorithm first captures the contour of ejected droplets at each time (figure 3*a*) and then tracks their position over time accounting for the unsteadiness of the problem. By superposing the contour of droplets from different frames on a single image, we can rebuild the trajectories of all ejected droplets experimentally (figure 3*b*), matching very well with the tracking results of our algorithm (figure 3*c*).

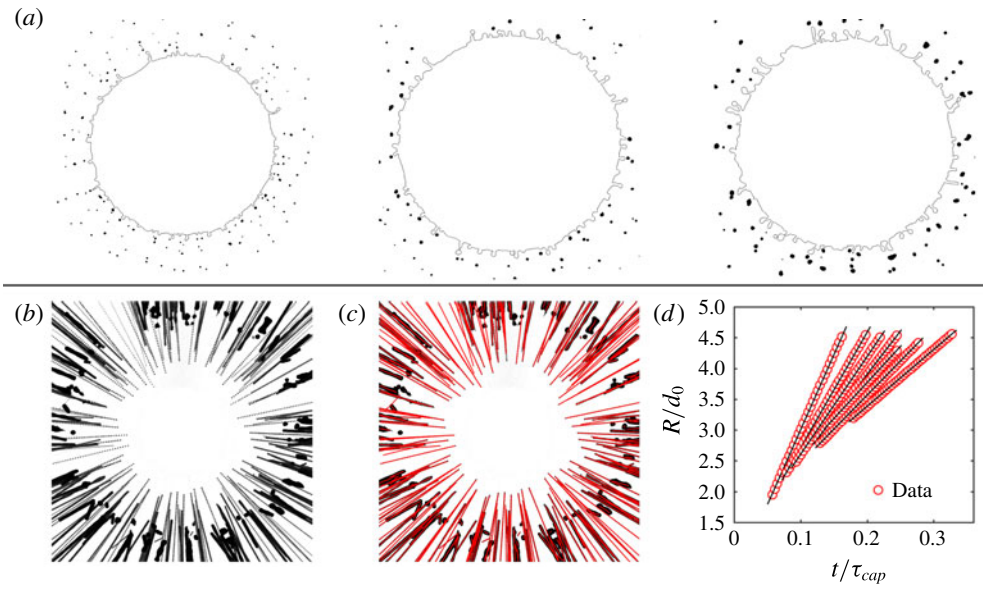

FIGURE 3. (Colour online) (*a*) Droplets detected by image processing at times $t = 0.2\tau_{cap}$, $t = 0.4\tau_{cap}$ and $t = 0.6\tau_{cap}$. The black line shows the outer contour of the rim and ligament. (*b*) Superposition of the trajectory of the droplets detected. (*c*) Tracks followed by each droplet. Solid lines indicate droplet trajectories captured by the algorithm. (*d*) Time evolution of the radial position of droplets with respect to the impact point, showing that the droplets move at constant speed.

As described above, the traditional approach to measuring the size of ejected droplets is to first detect their contour and then calculate their diameter from the enclosed area within the detected contour. Two factors affect the accuracy of drop size measurements. First, the contour on an image is detected from the gradient of the local intensity on the image. The pixels with highest local gradient around the object are considered part of its contour. Such a method has higher accuracy when the contrast between the object and the background is high and the object is well in focus, which we ensured. The error of measurement of our droplet sizes is of the order of a pixel size, with images of approximately 40 μm pixel^{-1}. The droplets ejected during fragmentation, except for the satellite droplets described in § 3, are larger than 0.4 mm with a measurement error smaller than 10 %. Second, the traditional approach used to compute droplet diameters based on the area A_d enclosed within the detected contour: $d_A = \sqrt{4A_d/\pi}$ is accurate when the droplet is spherical. Yet, the ejected droplets oscillate along their trajectories, under the balance of the inertia and surface tension (figure 4*a*). Figure 4(*b*) shows the time evolution of the droplet volume Ω_d calculated from the area-based diameter with $\Omega_d = \pi d_A^3/6$, clearly showing that such volume oscillates spontaneously, violating mass conservation. Since the evaporation time scale of droplets of $O(0.1$ mm) diameter is much larger than the fragmentation time scale, the volume of the droplet should remain constant within our duration of observation. The relative difference between the diameter of an oscillating droplet calculated from its area can reach up to 10 %, the same order of magnitude as that of a pixel-size error. The more accurate method of calculation of droplet diameter should be based on a volume estimation, that is constant over time, rather

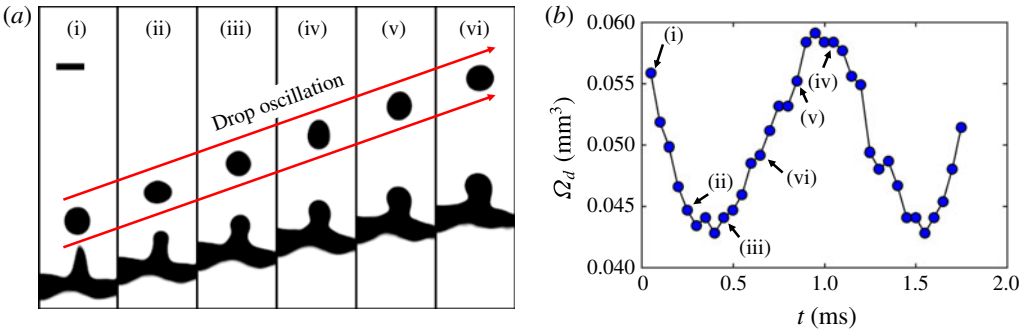

FIGURE 4. (Colour online) (*a*) Sequence of oscillation of a droplet after its detachment from its ligament of origin. The time interval between images is 0.2 ms and the scale bar is 0.5 mm. (*b*) Time evolution of the droplet volume Ω_d calculated from an area-based diameter $d_A = \sqrt{4A_d/\pi}$, where A_d is the area of the droplet shown in (*a*). $t = 0$ refers to the time at which the droplet detaches from the ligament. The data corresponding to the times shown in (*a*) are labelled in (*b*).

than area which changes with time. The two approaches are equivalent when the drop is exactly spherical. Our tracking algorithm detect the shape of each droplet and extract the times at which eccentricity is closest to 0 (spherical). The diameter is extracted from these selected times.

The speed of the droplets is obtained from calculation of the difference between the position of two consecutive frames. Two aspects affect the accuracy of such speed measurement. First, if a drop moves too fast, the droplet appears as a long blurred trajectory with low contrast. In order to capture such fast moving droplets, while not sacrificing image resolution, we reduce the shutter speed to 5 μs, 10 times higher than the frame rate, which enables us to capture droplets with velocities smaller than 10 m s^{-1}. The speed of the droplets ejected during unsteady sheet fragmentation are within this range. In fact, we do see tiny droplets ejected at the very early stage of sheet expansion of the order of 1 pixel size or less and leaving a blurred trajectory in the image, with very low contrast. The droplets on which our study focus are shed via a hydrodynamic instability of the expanding sheet in the air, while such very tiny droplets are ejected even when the sheet edge is still on the rod/solid surface, making the physics involved distinct, as no-slip, air trapping and precursor film ejections are involved. Our study does not focus on these tiny droplet closer to the micro-splashed droplets discussed in Thoroddsen *et al.* (2012) and Riboux & Gordillo (2015). The second aspect is the effect of pixelization. The accuracy for the droplet speed measurement from calculation of the difference between the droplet positions in two consecutive frames is 1 pixel/frame, corresponding to 0.8 m s^{-1} here, which could lead to large errors when the speed of droplets is less than that accuracy limit. To reduce the effect of pixelization, our algorithm can detect the time when the speed of droplets is smaller than that limit, and then re-calculates the speed by averaging the speed among multiple consecutive frames around that time. The smaller the droplet speed is, the more consecutive frames are needed to reduce the speed measurement error. The relative error for the speed measurement is reduced to up to 20 %.

Figure 3(*d*) shows the time evolution of the radial position of the ejected droplets with respect to the impact point, showing that droplets travel at a constant speed

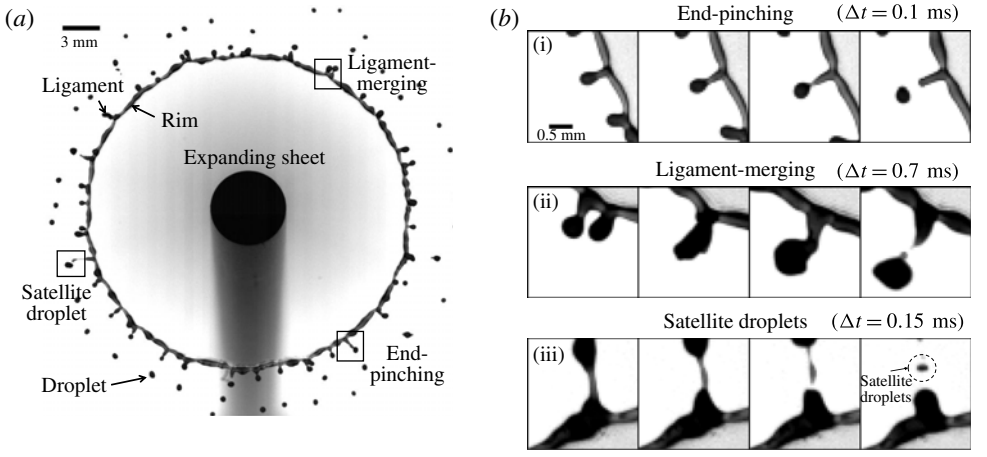

FIGURE 5. (*a*) Sheet fragmentation upon drop impact on a rod of comparable size to the impacting drop. The expanding sheet is bounded by a rim on which ligaments grow to finally eject secondary droplets. (*b*) Sequence of events for three different types of secondary droplet ejections: end-pinching, ligament-merging and satellite droplets.

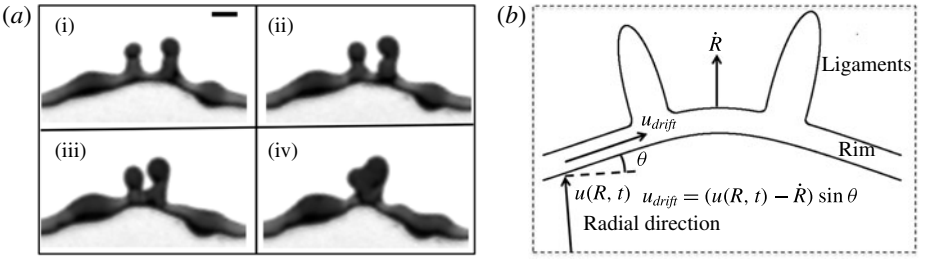

FIGURE 6. (*a*) Sequence showing the shift of ligaments induced by local cusps, leading to the collision and merger of two ligaments. Time difference between images is 0.25 ms. Scale bar is 1 mm. (*b*) Schematic diagram of drifting ligaments.

during our interval of observation. Since we are able to track the tip of a ligament as mentioned above, the same approach is used to measure the tip speed of ligaments. We discuss the relation between the speeds of droplets and ligament tips in § 5.

3. Three modes of droplet ejection

Drop shedding occurs continuously during sheet expansion in the form of three modes of droplet ejection (figure 5*b*). The first mode is end-pinching (figure 5*b*-i). Capillary deceleration of the tip of the ligament combined with fluid entering through the ligament foot leads to bulge formation at the tip. A neck forms between the bulged tip and the rest of the ligament and narrows progressively until a droplet is ejected. This mode was reported in prior studies of jets as end-pinching (Schulkes 1996; Gordillo & Gekle 2010; Hoepffner & Paré 2013).

The second mode of ejection is ligament-merging followed by end-pinching (figure 5*b*-ii). Ligaments do not always stay at a fixed angular position on the rim, but shift along it. Due to a local wedge geometry formed by the rim (figure 6). Such

wedge shape is similar to that around Savart sheets referred to as cusps (Gordillo, Lhuissier & Villermaux 2014). Cusps are caused by the non-uniform distribution of mass per unit arc-length. The fluid from the sheet entering the rim accumulates around corrugations and protrusions that can eventually become ligaments, at which point the increase in mass per unit arc-length reduces capillary deceleration locally, thus exacerbating local deformation (figure 6*a*). Around the cusps, the rim is no longer perpendicular to the incoming sheet radial influx, but is at an angle θ from it (figure 6*b*). Such angle induces a drift velocity along the rim. In the reference frame of the rim, the incoming velocity $u_{in}(t) = u(R(t), t) - \dot{R}(t)$, where $R(t)$ is the radius of the sheet at time t, $\dot{R}(t)$ is the radial velocity of the rim and $u(R(t), t)$ is the fluid velocity in the sheet at radius $R(t)$. The drift velocity induced is the projection of the incoming velocity u_{in} in the direction longitudinal to the rim:

$$u_{drift} = u_{in}(t) \sin\theta \quad \text{with } u_{in}(t) = u(R(t), t) - \dot{R}(t). \tag{3.1}$$

The velocity profile of the expanding sheet upon drop impact on a rod inferred from prior studies (Rozhkov, Prunet-Foch & Vignes-Adler 2004; Villermaux & Bossa 2011) and measured by Wang & Bourouiba (2017) is $u(r, t) = r/t$. In figure 6(*a*), we measure $u_{drift} \approx 0.32$ m s^{-1}, and we estimate $u_{in} = R(t)/t - \dot{R}(t) \approx 2.58$ m s^{-1}. The angle measured is $\theta \approx 8 \pm 2°$, giving a prediction of drift velocity $u_{drift} = 2.58 \times \sin(8) = 0.36$ m s^{-1} in good agreement with our experimental measurement. The shifting ligaments collide and merge (figure 5*b*-ii), resulting into a typically corrugated final ligament. Despite such corrugation, the resulting ligament continues to shed only one drop from its tip immediately upon merger. We refer to end-pinching and ligament-merging droplets as primary droplets.

The third mode of ejection creates satellite droplets (figure 5*b*-iii). During necking between the bulged tip and the rest of its ligament, the neck elongates and thins. Upon breakup, the neck can form one or multiple small satellite droplets. Such satellite droplets are much smaller than primary droplets produced by the first two modes and they account for only l0 % of all droplets ejected during sheet expansion. Thus, the satellite droplets are not involved in the discussion of the droplet size and speed distributions in subsequent sections.

4. Distribution of droplet sizes

4.1. *Cumulative size distribution of droplets*

Our study focuses on the size distribution of droplets ejected by the first two modes defined as primary droplets in § 3. They account for 90 % of the total number of droplets ejected during unsteady sheet fragmentation. Figure 7(*a*) shows the distribution of the diameter of primary droplets ejected during the entire sheet expansion. The distributions are skewed for all three Weber numbers. When attempting to fit them with a gamma distribution proposed in Villermaux, Marmottant & Duplat (2004)

$$P(n, x = d/\langle d\rangle) = \frac{n^n}{\Gamma(n)} x^{n-1} \mathrm{e}^{-nx}, \tag{4.1}$$

the order n changes severely with impact Weber number, departing from values given by Villermaux & Bossa (2011). Note that the underlying physics of (4.1) is that droplets fragment from elongated corrugated ligaments, where the coalescence and aggregation process of corrugations selects the droplet size distribution. As discussed

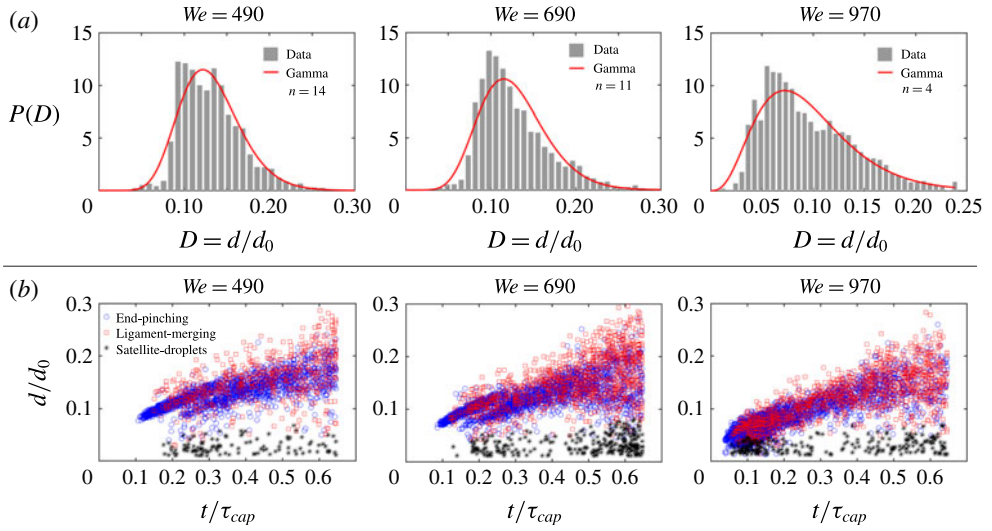

FIGURE 7. (Colour online) (*a*) Distributions of the diameter of primary droplets ejected during the entire fragmentation process for three different Weber numbers. Droplet diameters are non-dimensionalized by the diameter d_0 of the impacting drop. The distributions are all skewed and can be fitted by a gamma distribution of the order shown. (*b*) Temporal evolution of the diameter of ejected droplets for three different Weber numbers. Time is non-dimensionalized by the capillary time scale $\tau_{cap} = \sqrt{\rho\Omega/\pi\sigma}$. Each data point corresponds to one ejected droplet. Ejected droplets are separated into the three groups described in figure 5(*b*).

in § 3, here a ligament only sheds one droplet from its tip at a time in an end-pinching process. Thus, aggregation–coalescence of corrugations along ligaments do not apply to rationalize the drop size distribution of unsteady expanding sheets examined here.

Figure 7(*b*) shows the measured diameters of ejected droplets with their detachment time. Time is non-dimensionalized by the capillary time scale $\tau_{cap} = \sqrt{\rho\Omega/\pi\sigma}$ that characterizes the sheet expansion and fragmentation process, where Ω is the volume of the impacting drop. Each data point corresponds to one ejected droplet. Ejected droplets are separated into the three ejection modes described in § 3. Except for the less than 10 % of all droplets that are shed as satellite droplets, the mean diameter of primary droplets clearly increases with time (figure 8*b*). Thus, it is the superposition of distributions with shifting mean that leads to the skewed total distribution of droplet sizes (figure 3*a*). To verify this, we calculate the instantaneous distribution of primary droplet diameters at each time by considering data around that time over a small time interval of 0.15 ms duration, within which the unsteadiness of the sheet fragmentation is negligible. Figure 8 shows that the instantaneous distribution at each time is symmetric and Gaussian. Figure 8(*c*) shows the *total* distribution of diameters of ejected droplets after subtraction of the instantaneous mean diameter shown in figure 8(*b*). The total distribution adjusted by its unsteady instantaneous mean diameter is symmetric. This verifies that the skewness of the total distribution shown in figure 7(*a*) is caused by the unsteady temporal evolution of instantaneous mean droplet diameters.

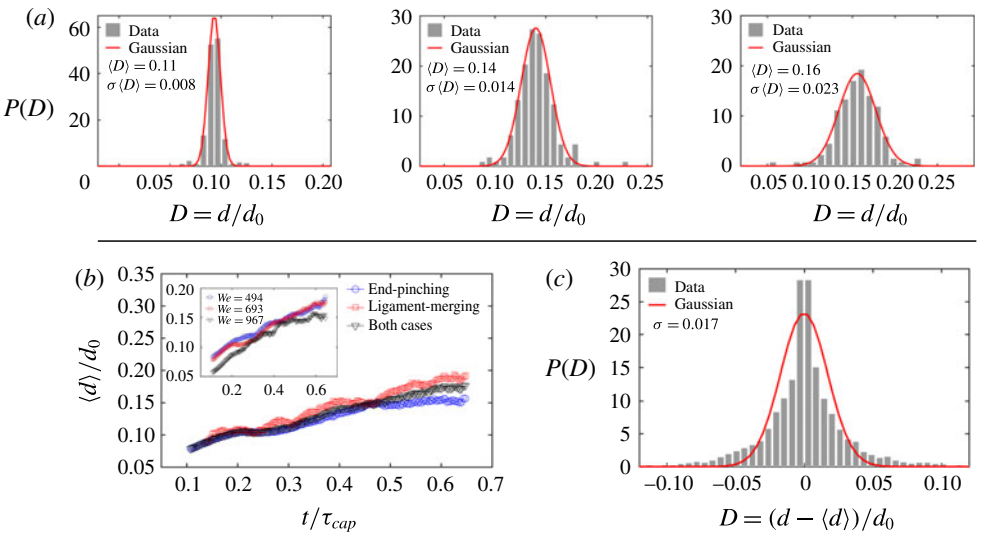

FIGURE 8. (Colour online) (*a*) Instantaneous distributions of the diameter of primary droplets at three different times $t = 0.2\tau_{cap}$, $0.4\tau_{cap}$ and $0.6\tau_{cap}$ for $We = 693$, where $\tau_{cap} = \sqrt{\rho\Omega/\pi\sigma}$ is the capillary time scale characterizing the sheet expansion and fragmentation process, and $t = 0.4\tau_{cap}$ is the time when the sheet reaches its maximum extension. The instantaneous distributions are symmetric and Gaussian. (*b*) Time evolution of the mean diameter of droplets from different ejection modes for $We = 693$. The inset shows the comparison of the mean diameters of primary droplets for three different We. (*c*) The total distribution of the diameter of all primary ejected droplets for $We = 693$ after adjustment for the instantaneous mean diameter is not skewed.

4.2. *End-pinching ligament width shapes droplet diameter*

Discovering that unsteadiness shapes the skewness of the total distribution of droplet diameters, we examine the time evolution of the population mean droplet diameter $\langle d\rangle$. As discussed in § 3, droplets are mainly ejected from ligament tips. Our tracking algorithm (§ 2) allows us to link each ejected droplet to its original ligament. Figure 9(*a*) shows the ratio, $R = d/w$, of the diameter d of ejected droplet to the width w of its original ligament as a function of time. Except for satellite droplets again, less than 10 % of total droplets, the mean droplet–ligament size ratio for primary droplets is constant over time: $\langle R\rangle = \langle d/w\rangle \approx 1.5$ (figure 9*b*), and is independent of impact Weber number (inset of figure 9*b*). This shows that the diameter of droplets is determined deterministically by the width of the ligament shedding them, and that such droplet–ligament size ratio is local and universal, i.e. independent of impact We and sheet expansion.

In the case of a long cylindrical liquid ligament, the Rayleigh–Plateau instability (Rayleigh 1878) typically triggers fragmentation with a fastest growing wavelength of $\lambda = 9w/2$, where w is the initial cylinder diameter. Based on mass conservation, the volume of the produced droplets at such wavelength would be

$$\frac{\pi}{6}d^3 = \frac{9}{2}w\left(\frac{1}{4}\pi w^2\right), \quad \text{thus } \frac{d}{w} = 1.89, \tag{4.2}$$

which is larger than $\langle R\rangle = \langle d/w\rangle \approx 1.5$. However, the Rayleigh–Plateau (R–P) instability strictly holds for infinite or semi-infinite liquid cylinders. As discussed

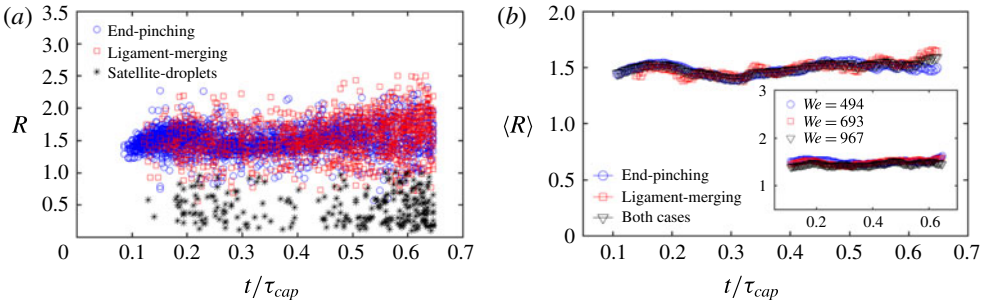

FIGURE 9. (Colour online) (*a*) The ratio R of the diameter d of each secondary droplet with the width w of its original ligament as a function of detaching time for $We = 693$. Droplets are separated into three scenarios as described in figure 5(*b*). (*b*) Time evolution of the mean droplet–ligament size ratio of ejected droplets of different scenarios for $We = 693$. The ratio R of primary droplets remain constant over time. The inset shows that ratio $\langle R \rangle \approx 1.5$ holds for all We.

in § 3, droplets ejected during sheet fragmentation are shed from the tip of finite ligaments that are too short for the R–P instability to apply. Instead, droplets are shed via end-pinching which is caused by the retraction of ligament tips. Schulkes (1996) studied end-pinching numerically for free liquid jets of arbitrary viscosity, finding that the evolution of the ligament tip depends on the Ohnesorge number $Oh = \nu\sqrt{\rho/w\sigma}$, a measure of competition between viscous forces, inertia and surface tension, similar to the retraction of the rim of a sheet (Savva & Bush 2009). Ligaments of large Ohnesorge number $O(Oh) > O(1)$ are stable during retraction, while ligaments of small Ohnesorge number $O(Oh) < O(0.1)$ form a neck close to the ligament tip. When Oh is much smaller $O(Oh) < O(0.001)$, the ligament is unstable and the neck narrows quickly until end-pinching. The critical value of Oh below which end-pinching occurs was found to be $Oh \approx 10^{-2}$ (Schulkes 1996). Based on the width of ligaments shown in figure 11, the range of Oh here is $5.3 \times 10^{-4} < Oh < 8.5 \times 10^{-3}$, for which end-pinching holds. A fully analytic solution describing end-pinching remains elusive since vortex shedding was observed to occur experimentally at ligament tips during necking (Hoepffner & Paré 2013), jeopardizing the validity of a one-dimensional approximation of the problem (Eggers & Dupont 1994). Schulkes (1996) found numerically that the ratio of the diameter of a droplet ejected by end-pinching to the width of its ligament of origin is 1.5–1.6, which is close to our experimental data (figure 9).

Gordillo & Gekle (2010) studied end-pinching at the tip of a Worthington jet, which is a stretched liquid jet. Stretching rate can affect the ligament-tip breakup. Scaling analysis compared with numerical simulation led Gordillo & Gekle (2010) to quantify R as

$$R = \frac{d}{w} = \begin{cases} 0.95 We_s^{-1/7} & \text{for } We_s > 0.08 \\ 1.55 & \text{for } We_s < 0.08 \end{cases} \quad \text{with } We_s = \frac{\rho w^3}{8\sigma} s_0^2, \tag{4.3}$$

where s_0 is the stretching rate of the ligament $s_0 = \dot{u}_{liga}/u_{liga}$, with u_{liga} the velocity of fluid entering the base of the ligament. Equation (4.3) indicates that when $We_s > 0.08$, the ligament is dominated by stretching and the droplet–ligament size ratio R is affected by said stretching. In our experiments, we estimate that for each

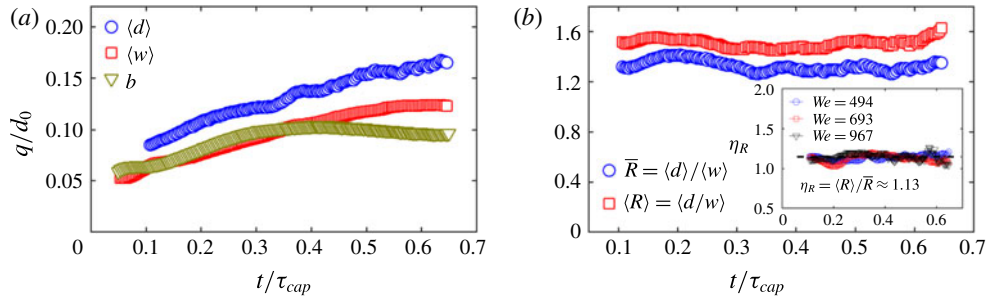

FIGURE 10. (Colour online) (*a*) Time evolution of the mean droplet diameter $\langle d\rangle$, the mean ligament width $\langle w\rangle$ and the sheet rim thickness b for $We = 693$. (*b*) The ratio $\bar{R} = \langle d\rangle/\langle w\rangle$ remains constant. However, compared with the mean size ratio of droplet–ligament pairs $\langle R\rangle = \langle d/w\rangle$, a systematic gap between these two ratios persists. The inset shows the ratio of $\eta_R = \langle R\rangle/\bar{R}$ to be constant over time and independent of *We*, with a value of 1.13.

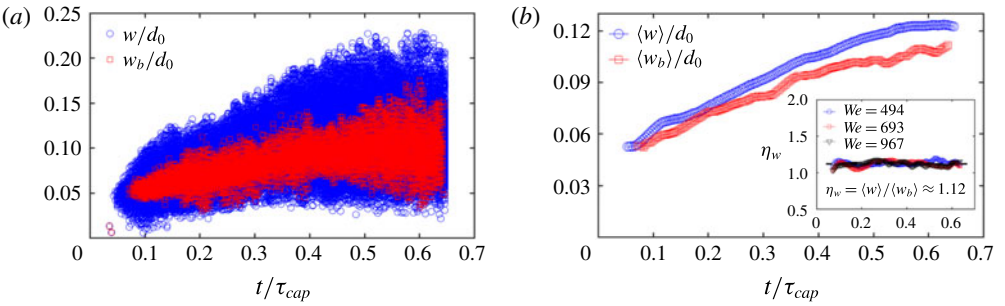

FIGURE 11. (Colour online) (*a*) Width of all ligaments (circle) w and ligaments about to shed a droplet (square) w_b as a function of time. (*b*) Time evolution of the corresponding mean widths $\langle w\rangle$ and $\langle w_b\rangle$. The inset shows the ratio $\eta_w = \langle w\rangle/\langle w_b\rangle \approx 1.12$ to be constant and independent of *We*.

ligament $We_s \approx 0.05$, below the stretching regime of $We_s > 0.08$. Using (4.3), the droplet–ligament size ratio would then be $R = d/w = 1.55$, in good agreement with our experiments.

In sum, we showed that the droplet ejection from unsteady sheet expansion is caused by end-pinching, rather than the R–P instability or corrugation–coalescence process of individual ligaments. We also showed that the droplet–ligament size ratio of end-pinching obtained numerically in prior literature on jets applies and is robust herein for the ligaments bounding the unsteady rim.

After considering the drop–ligament size ratio for each droplet–ligament pair, we now turn to the relation between the population mean droplet diameter $\langle d\rangle$ and the population mean ligament width $\langle w\rangle$ (figure 10*a*). It is clear that the mean droplet diameter $\langle d\rangle$ follows the same trend as the mean ligament width $\langle w\rangle$, consistent with figure 9. Figure 10(*b*) shows $\bar{R} = \langle d\rangle/\langle w\rangle \approx 1.3$ to be constant over time, but systematically smaller than $\langle R\rangle = \langle d/w\rangle \approx 1.5$. The difference between the two $\eta_R = \langle R\rangle/\bar{R} \approx 1.12$ is constant and independent of Weber number (figure 10*b*-inset). To understand the gap η_R, we examine the width of ligaments during droplet shedding in more detail.

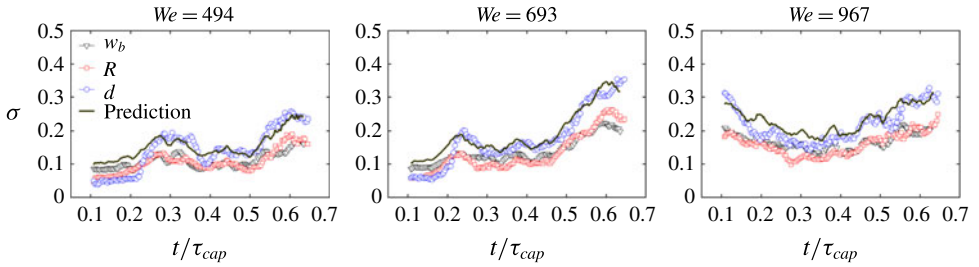

FIGURE 12. (Colour online) Comparison of time evolution of the standard deviation of the width of shedding ligaments w_b, droplet–ligament size ratio R and droplet diameter d. The prediction of $\sigma(d)$ based on (5.3) is in very good agreement with the measurement.

Figure 11(*a*) shows the temporal evolution of the width w of all ligaments detected compared to the width w_b of those ligaments about to shed a drop, with their means shown in figure 11(*b*). The systematic gap between the two means $\eta_w = \langle w\rangle/\langle w_b\rangle \approx 1.12$ is also constant and independent of Weber number (figure 11*b*-inset), and equal to the ratio $\eta_R = \bar{R}/\langle R\rangle$. Thus, the difference between the mean droplet–ligament size ratio of each droplet–ligament pair $\langle R\rangle = \langle d/w\rangle$ and the ratio of the population mean droplet diameter with the population mean ligament width $\bar{R} = \langle d\rangle/\langle w\rangle$ is caused by the systematic difference in width between shedding $\langle w_b\rangle$ and non-shedding ligaments $\langle w\rangle$. Ligaments about to shed a drop generally have time to extend into a slender shape, while non-shedding ligaments are typically close to bulged corrugations that are wider. Clarifying the origin of the particular value 1.12 of $\langle w\rangle/\langle w_b\rangle$ for end-pinching ligaments is of interest, but is beyond the scope of the present study.

Figure 9 shows the standard deviation of the width w_b of ligaments that eject droplets, the size ratio of droplet–ligament pairs R and the diameter of droplets d as a function of time. Considering the mean $\langle R\rangle$ and $\langle w_b\rangle$ and standard deviation $\sigma(R)$ and $\sigma(w_b)$ and, using $d = Rw_b$, the standard deviation of the droplet diameter $\sigma(d)$ is

$$\sigma^2(d) = (\sigma^2(R) + \langle R\rangle^2)(\sigma^2(w_b) + \langle w_b\rangle^2) - \langle R\rangle^2\langle w_b\rangle^2. \tag{4.4}$$

The prediction of standard deviation of ejected droplet diameter by (4.4) is in a good agreement with our experimental data (figure 12), confirming the robustness and accuracy of our measurements. Equation (4.4) combined with figure 10(*b*) show that the standard deviation of instantaneous droplet diameter around their mean size is directly inherited from the standard deviation of the width of their ligament of origin at breakup, and not from the breakup process itself.

5. Distribution of droplet ejection speed

5.1. *Cumulative speed distribution of droplets*

Figure 13(*a*) shows the total speed distribution of droplets ejected throughout the unsteady sheet fragmentation for three different Weber numbers, non-dimensionalized by impact velocity u_0. The total distribution of droplet speeds has a peculiar shape with two peaks. Figure 13(*b*) shows the measured speed of all ejected droplets, as a function of their detaching time, for three *We*. As previously done, time is non-dimensionalized by the capillary time scale $\tau_{cap} = \sqrt{\rho\Omega/\pi\sigma}$, which is characteristic of the sheet expansion and fragmentation. Ejected droplets are separated

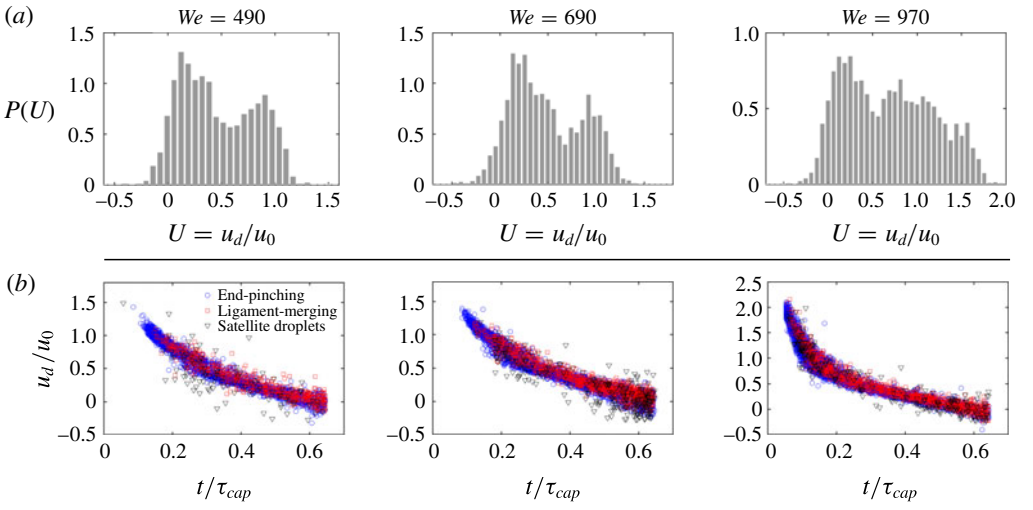

FIGURE 13. (Colour online) (*a*) Total distribution of speed of droplets ejected during the entire fragmentation process for three different Weber numbers (a Weber per column). The droplet speed distribution is non-dimensionalized by the impact speed u_0 of the falling drop. (*b*) Ejection speed of droplets as a function of time for three different Weber numbers with each data point corresponding to one ejected droplet. Ejected droplets are separated into the three different modes of ejections revealed in § 3.

in the three modes of ejection: end-pinching, ligament-merging and satellite droplet ejection identified in § 3. The ejection speed of droplets varies with time (figure 13*a*) and is monotonically decreasing with time. Clearly, the total speed distribution is entirely shaped by the unsteadiness of the instantaneous mean of the ejection droplet speed. To verify this claim, we calculate the distribution of droplet ejection speed at each time as shown in figure 14(*a*). The instantaneous distribution is symmetric and Gaussian. Figure 14(*b*) shows the time evolution of the standard deviation of the ejection speed of droplets for different modes of ejection. Both the mean value and standard deviation of the ejection speed of end-pinching and ligament-merging droplets collapse onto a single curve, showing that the ejection speed is independent of the mode of ejection (figure 14*b*,*c*).

Figure 15 shows the total distribution of the ejection speed of droplets after subtraction of the instantaneous mean speed (figure 14*b*). The total adjusted distribution is symmetric and Gaussian. Thus, the peculiar shape of droplet speed distribution in figure 13 is due to the unsteadiness of the mean of ejection speed characterized by two regimes: an early time and late time speed evolution. Figure 15(*b*,*c*) shows that the total speed distribution of both end-pinching and ligament-merging droplets around their respective mean speeds are also Gaussian, confirming that the instantaneous ejection speed of droplets is independent of ejection mode.

5.2. *Ligament speed shapes droplet speed*

It is important to understand what determines the time evolution of mean droplet ejection speeds. Figure 16(*a*) shows that ligament-tip speed and droplet ejection speed fully overlap. This indicates that the drop ejection speed is determined by the speed of the tip of its ligament. Keller (1983) studied the retraction speed of the tip

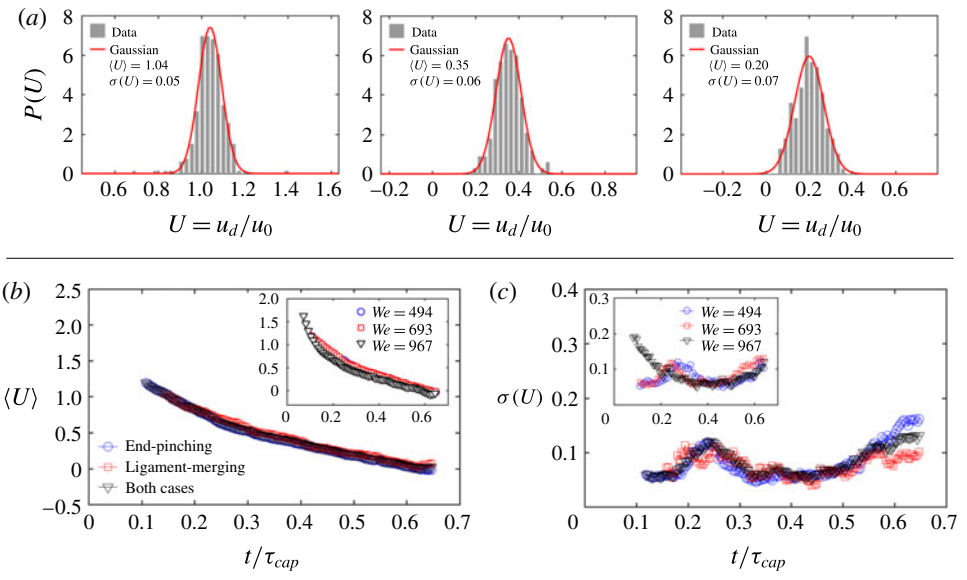

FIGURE 14. (Colour online) (*a*) Instantaneous distribution of droplet speed at three different times $t = 0.2\tau_{cap}$, $0.4\tau_{cap}$ and $0.6\tau_{cap}$ for $We = 693$, where $\tau_{cap} = \sqrt{\rho\Omega/\pi\sigma}$ is the capillary time scale characterizing the sheet expansion. $t = 0.4\tau_{cap}$ is the time of maximum sheet radius. Instantaneous speed distributions are Gaussian with standard deviation given in the legend. (*b*) Mean ejection speed and (*c*) associated speed standard deviation of the droplets follow the same temporal trend for both end-pinching and ligament-merging modes of ejection.

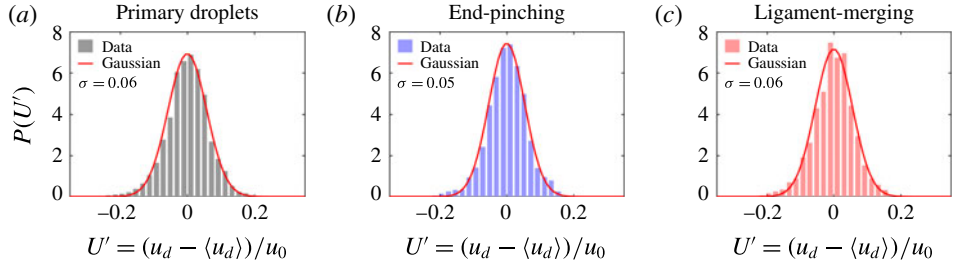

FIGURE 15. (Colour online) (*a*) The total distribution of ejection speeds of all droplets for $We = 693$ after adjustment for instantaneous mean speed is Gaussian in contrast with the total speed distribution in figure 13. Clearly, unsteadiness of the instantaneous mean droplet speed shapes the skewness observed in figure 13. The same applies for the speed of (*b*) end-pinching and (*c*) ligament-merging droplets when considered separately.

of free liquid jets and derived, by momentum conservation, that the tip retraction speed is constant $\sqrt{2\sigma/r_l}$ for uniform liquid jets of radius r_l, which is similar to a Taylor–Culick speed for ruptured sheet retraction (Culick 1960). Hoepffner & Paré (2013) showed that the retraction tip speed of free liquid jets should be $\sqrt{\sigma/r_l}$, which was verified by their own experimental data. The expression of Keller (1983) overestimates the speed by a factor of $\sqrt{2}$ due to their neglect of the inner curvature pressure of the cylindrical liquid jet, which was recovered in their derivation for the

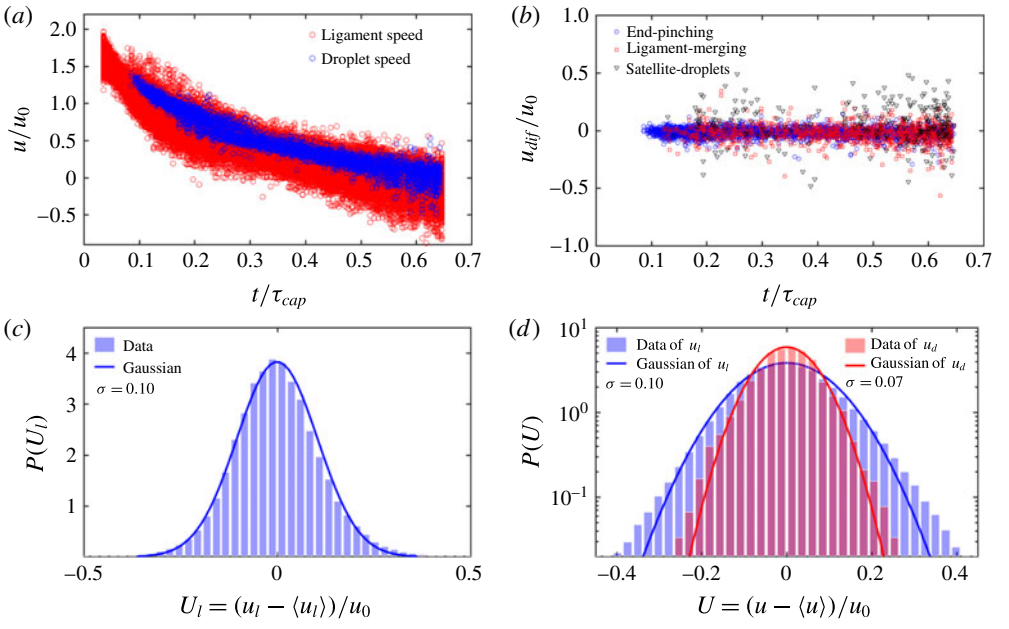

FIGURE 16. (Colour online) (*a*) Temporal evolution of ejection speed of droplets and tip speed of ligaments. The overlap between the two shows that the speed of a ligament tip is inherited by the droplet right after detachment. (*b*) Zero velocity difference between the ejection speed of droplets and the tip speed of their ligaments of origin. (*c*) The total distribution of ligament-tip speeds adjusted for the moving instantaneous mean is symmetric and Gaussian. (*d*) Comparison of the distribution of ligament-tip speeds adjusted for the moving mean, as shown in (*c*), with that of the ejection speed of primary droplets, as shown in figure 15(*a*), on a semi-log plot, both being Gaussian. The width of the distribution of ligament-tip speeds is larger than that of primary droplet speeds.

speed of the jet tip in Ting & Keller (1990). However, as shown in figure 16, the tip speed of a ligament growing out of a rim here is not constant. Instead, it follows the speed of the sheet rim. Indeed, the incoming fluid from the rim into the base of the ligament is determined by both the sheet expansion and rim destabilization. Based on our ligament-tracking algorithm introduced in § 2, we can link each droplet to the ligament from which it detaches. Figure 16(*b*) shows no distinction between the speed of a droplet and that of the ligament from which it detaches. That is, the ejection speed of each droplet is equal to the speed of its ligament's tip prior to breakup.

Although the droplet speed is equal to the ligament-tip speed prior to detachment for each droplet–ligament pair, a systematic gap between the population mean ejection speed of droplets and the population mean speed of ligament tips exists (figure 18*a*). To understand the origin of such gap, we need to examine the detachment more precisely.

Figure 17(*a*) shows the ligament deformation preceding droplet detachment in the form of a sequence. All images are given in the reference frame of the ligament. As described in § 4, capillary forces decelerate the tip of the ligament, while fluid continues to feed its foot, thus leading to fluid accumulation forming a bulged tip. A neck forms between the tip and the rest of the ligament. The neck width narrows

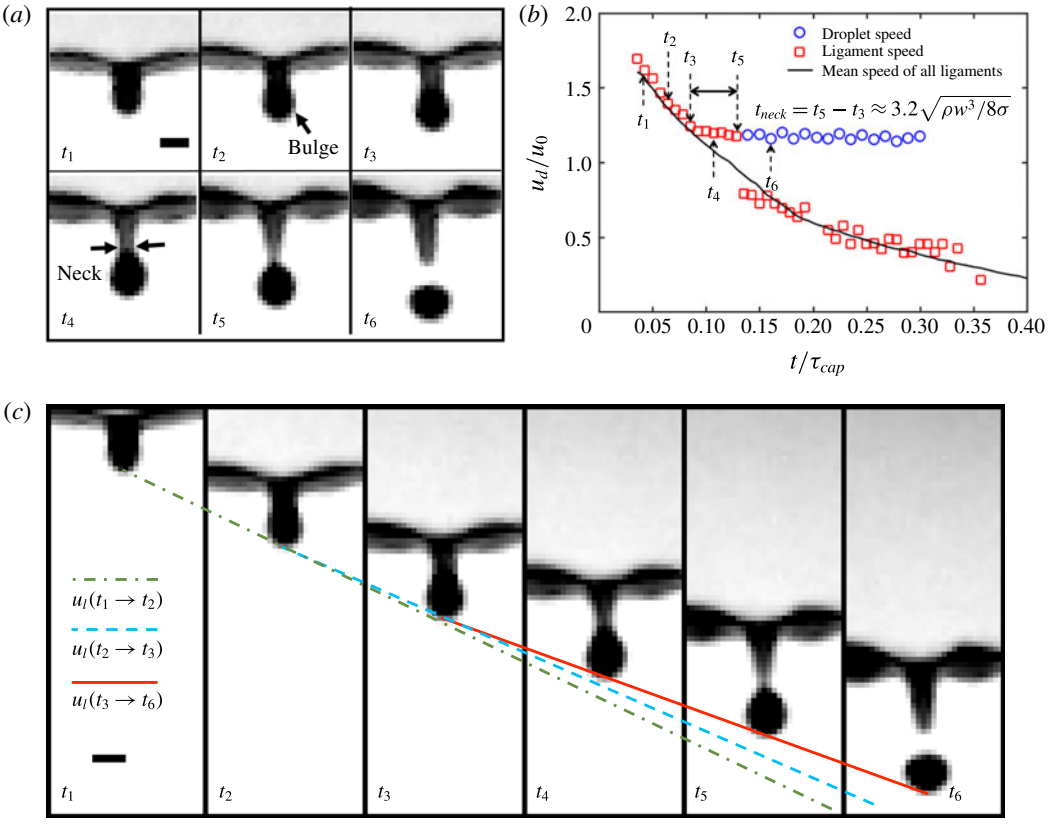

FIGURE 17. (Colour online) (*a*) Sequence of events leading to bulge formation and necking of the tip of the ligament prior to droplet detachment in the reference frame of the rim. t_3 is the time of start of necking, and t_5 is the time of droplet ejection. The time interval between images is 0.15 ms and the scale bar is 0.3 mm. (*b*) Time evolution of the tip speed of one ligament and the ejection speed of the secondary droplet detaching from it. The solid line gives the time evolution of the population mean speed of all ligament tips. (*c*) Sequence of ligament deformation prior to droplet detachment in the absolute reference frame. t_1 to t_6 correspond to the times shown in (*a*). The solid line shows that after necking, the ligament tip moves at constant speed, which is the same as the ejection speed of droplets after detachment. The dot-dash line connects the tip positions at t_1 and t_2 and the dash line connects the tip positions at t_2 and t_3. By comparing the slopes of the three lines, it is clear that the ligament tip decelerates before necking at t_3, which is consistent with (*b*). Scale bar is 0.3 mm.

progressively to finally break and eject a droplet. In figure 17(*a*), the ligament continues to grow on the rim at time t_1. When time t_2 is reached, the ligament tip deforms into a bulge. At time t_3, the bulged tip of the ligament is fully formed and the neck between the bulged tip and the ligament starts to form. Compared to the ligament at time t_4 where a clear neck is observed, the ligament maintains an approximate constant width between the bulged tip and the rim at time t_3. Thus we consider t_3 as the onset of neck formation. At time t_5, the width of the neck narrows down to 0, the ligament is close to pinching and ejection of the droplet. At time t_6, the droplet is ejected by the ligament and moves freely in the air. Figure 17(*b*) shows

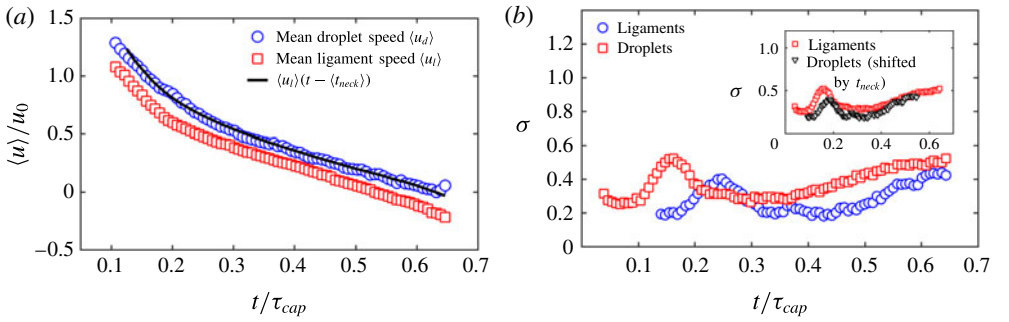

FIGURE 18. (Colour online) (*a*) Normalized time evolution of the population mean speed of secondary droplets (blue circle) compared with the population mean speed of ligament tip (red square) for $We = 693$. The velocity gap between the two is due to ligament necking. The mean speed of ligaments one necking time t_{neck} (5.2) earlier (dash line) matches very well with the mean speed of droplets. (*b*) The standard deviation of the speed of secondary droplets follows the trend of ligament-tip speed, but also with a time delay of t_{neck}. When shifted by t_{neck}, the standard deviation of droplet speed matches with that of ligament-tip speed (inset). This confirms that the speed evolution of secondary droplets is inherited from the ligament tip one necking time earlier.

the time evolution of the speed of one ligament's tip (figure 17*a*), compared to the population mean speed of ligament tips. From neck formation until final breakup, the speed of the ligament tip deviates from the population mean tip speed but remains constant, and equal to the final droplet ejection speed. This is readily observed when we look at the motion of ligaments in the absolute reference frame. Figure 17(*c*) shows the solid straight line which crosses the tip of the ligament from t_3 to t_5, indicating that the tip speed remains constant throughout the duration of necking. The solid line also crosses the lower end of the ejected droplet at time t_6. This shows that the constant speed of the ligament tip during necking is equal to the speed of the ejected droplet, which is consistent with figure 17(*b*). We can also see that the slope of the solid line is smaller than that of the dash line connecting the tip positions at t_2 and t_3 and the dot-dash line connecting the tip position at t_1 and t_2, showing that the tip is decelerating before necking t_3. Indeed, when the neck narrows, the capillary force exerted by the neck on the ligament tip, $F \approx \sigma \pi w_n$, decreases, where w_n is the width of the neck. Hence, the decrease of the capillary-induced deceleration of the tip.

Since the speed of a droplet is equal to the speed of the tip of its ligament of origin, which remains constant throughout necking, the droplet ejection speed should be equal to the ligament-tip speed one necking time prior to pinch-off. Thus, the population mean speed of droplets and ligaments should relate as:

$$\langle u_d \rangle = \langle u_l \rangle (t - \langle t_{neck} \rangle), \tag{5.1}$$

where t_{neck} is the necking time of the ligament. Dimensional analysis allows to estimate the necking velocity as $v_n \sim \sqrt{\sigma/\rho w}$, where w is the width of the ligament and is also the local characteristic length scale of the necking region. The necking time scale is $t_n \sim w/v_n = \sqrt{\rho w^3/\sigma}$, showing that the necking time scale t_n is proportional to the local capillary time scale, which has been reported in prior studies of breakup of free cylindrical liquid jets (Sterling & Sleicher 1975; Eggers & Dupont

1994; Gordillo & Perez-Sborid 2005). Clanet & Lasheras (1999) experimentally measured the necking time of a drop pinching-off from a nozzle and found its empirical expression to be

$$t_{neck} = 3.16\sqrt{\frac{\rho w^3}{8\sigma}}. \tag{5.2}$$

This result is close to the characteristic growth time scale of the fastest growing mode of the R–P instability (Rayleigh 1878) for free cylindrical liquid columns, which has the same expression as (5.2) with prefactor 2.91 instead of 3.16. Schulkes (1996) and Gordillo & Gekle (2010) studied the breaking time of a drop from the tip of a retracting ligament by end-pinching. In their numerical simulations, they found that the breaking time for an inviscid and unstretched ligament is $t_{break} \approx 4.7\sqrt{\rho w^3/8\sigma}$, larger than the necking time (5.2) obtained by Clanet & Lasheras (1999). Our experimental data show a necking time $t_{break} \approx 3.2\sqrt{\rho w^3/8\sigma}$, which is very close to (5.2), but smaller than the breaking time obtained by Schulkes (1996) and Gordillo & Gekle (2010). Indeed, we consider the necking time as the period of narrowing of the neck during which the tip speed remains constant, while the breaking time obtained numerically by Schulkes (1996) and Gordillo & Gekle (2010) refers to the full duration from a uniform ligament to final breakup of its neck, including the early stage of bulge formation. In order to verify (5.1), we compute the mean necking time of ligaments based on (5.2) and use the measured mean width of ligaments. As described in § 4.2, we introduced two different types of mean ligament widths: the mean width of all ligaments on the rim $\langle w \rangle$, and the mean width of ligaments about to shed a droplet $\langle w_b \rangle$. Ligaments about to shed droplets extend into slender bodies before the shedding. Thus, $\langle w_b \rangle$ is systematically smaller than $\langle w \rangle$ during fragmentation, with a robust and Weber-number-independent ratio $\eta_b = \langle w \rangle / \langle w_b \rangle \approx 1.12$. Here, since t_{neck} refers to the necking time of the ligament about to shed a droplet, we need to use w_b, rather than w for the calculation of t_{neck}. Using (5.1) and (5.2), our prediction of the mean speed of droplets is in excellent agreement with our experimental data shown in figure 18(*a*). In addition to the mean speed of droplets and ligaments, figure 18(*b*) shows that the standard deviation of the distribution of droplet speeds follows the same trend as the standard deviation of the distribution of ligament-tip speeds, but appears delayed. When shifted by one population mean necking time $\langle t_{teck} \rangle$, the standard deviation of the speed of the droplets also matches that of the speed of the ligament tips well. Combining the results of figure 18(*a*,*b*), we confirm that the population mean ejection speed of droplets is the population mean speed of ligament tips one necking time prior to pinch-off.

6. Conclusion

Unsteady fluid fragmentation is ubiquitous in nature and important to control in a range of industrial and environmental processes. To date, the literature mainly focused on the size distribution of fragmented droplets. By contrast, little attention has been paid to the droplet speed distribution, though the speed of droplets is critical for chemical and pathogen transport, shaping the range and severity of contamination. Even for droplet size distributions, various models were proposed for steady fragmentation (Villermaux 2007), yet few studies focused on unsteady fragmentation. Here, we studied both the size and speed distributions of droplets ejected during canonical unsteady sheet fragmentation upon drop impact on a

surface of comparable size to that of the impacting drop. The insights gained in this canonical problem are important as they can be generalized to more complex unsteady fragmentation processes.

We developed high-precision image processing and tracking algorithms that capture all ejected droplets, measuring their sizes and speeds, as well as their detaching times and ligaments of origin. We showed three ejection modes of droplets from ligament breakup: end-pinching, ligament-merging followed by end-pinching and satellite droplets. Each ligament sheds one drop at a time in the first two modes, which account for the creation of over 90 % of the droplets. We also found that the total size and speed distributions of droplets ejected during unsteady sheet fragmentation are skewed. Such skewness is due to the unsteadiness of the sheet expansion, inducing an increase of the population mean diameter and a decrease of the population mean speed of droplets shed throughout the sheet expansion. The instantaneous size and speed distributions remain, however, symmetric and Gaussian. It is the superposition of Gaussian distributions with moving means that give rise to the skewness of the total size and speed distributions observed.

For droplet sizes, we showed that the ratio of diameter of each ejected droplet to the width of its ligament of origin, at a given time, is $\langle R\rangle = \langle d/w\rangle \approx 1.5$, and is constant and independent of impact Weber number. The mean instantaneous droplet diameter $\langle d\rangle$ is selected by the instantaneous ligament width $\langle w\rangle$ that increases over time. The droplet-ligament size ratio $\langle R\rangle = \langle d/w\rangle = 1.5$ differs from that expected from the Rayleigh–Plateau instability, but is consistent with the ratio obtained numerically for jet end-pinching (Schulkes 1996; Gordillo & Gekle 2010). Although the droplet–ligament size ratio $\langle R\rangle = 1.5$ is robust for each droplet–ligament pair, we found a systematic gap between $\bar{R} = \langle d\rangle/\langle w\rangle$ and $\langle R\rangle = \langle d/w\rangle$: $\eta_R = \langle R\rangle/\bar{R} = 1.12$. We showed that this is due to the gap between the instantaneous mean width of all ligaments $\langle w\rangle$ and the instantaneous mean width of ligaments about to shed a drop $\langle w_b\rangle$. At each time, the ligaments about to shed a drop are more slender than the others with $\eta_w = \langle w\rangle/\langle w_b\rangle = 1.12$, a value we found to be robust, constant and independent of impact *We*.

For droplet speeds, we showed that the ejection speed of droplets is equal to the tip speed of their ligaments of origin prior to necking onset for each droplet–ligament pair. We showed that, during necking, the tip speed of a ligament remains constant, but deviates from the population mean speed of ligament tips that continues to decelerate with the sheet rim. In fact, the population mean speed of droplets is equal to the population mean speed of ligaments one necking time earlier.

In sum, our findings show the critical importance of unsteadiness in shaping both size and speed distributions of fragmented droplet sprays. For unsteady fragmentation, the size and speed of droplets ejected by their ligament, one at a time via end-pinching, evolve continuously; hence resulting in a final cumulative polydisperse distribution. This is in contrast with the mechanism of aggregation–coalescence of corrugated long ligaments producing multiple droplets for steady ligament-mediated fragmentation. Thus, when both unsteadiness and aggregation–coalescence processes coexist at different stages or simultaneously during fragmentation, it is important to examine which of the two effects dominate in selecting for the skewness of the final drop speed and size distributions. A blind fit of distributions, including gamma distributions such as (4.1), can lead to misleading insights into the underlying physics and limit predictability and control of spray properties for changing conditions of operation. In the ubiquitous case of sheet fragmentation upon drop impact considered herein, the fragmentation is coupled with the unsteady sheet expansion. Time evolution

of sheet expansion upon drop impact on solid surfaces or small targets were studied (Yarin & Weiss 1995; Rioboo, Marengo & Tropea 2002; Rozhkov, Prunet-Foch & Vignes-Adler 2002; Roisman, Berberovi & Tropea 2009; Eggers *et al.* 2010; Villermaux & Bossa 2011; Lastakowski *et al.* 2014). However, few studies attempted to link the dynamics of sheet expansion to the fragmented droplets. Some did so focusing on the droplet sizes and the later stage of retraction (Villermaux & Bossa 2011) and others at the very early stage prior to full sheet formation (Riboux & Gordillo 2015). The dynamics that links the sheet, to the rim, to the ligaments and to the final droplet sizes and speeds throughout the entire unsteady sheet expansion remains unknown. This paper links the size and speed of ligaments with the size and speed of their ejected droplets throughout the entire unsteady sheet expansion. The full dynamics coupling the unsteady sheet–rim–ligament system is our next focus. Finally, this fundamental study also has profound implications for the understanding and control of fluid fragmentation leading to pathogen transmission from contaminated finite surfaces (Gilet & Bourouiba 2014, 2015; Wang & Bourouiba 2018), and efficacy of coating or washing of such surfaces, in addition to the myriad of other industrial and agricultural processes involving sprays.

Acknowledgements

This research was supported in part by the USDA-NIFA Specialty Crop Research Initiative Grant Award No. MDW-2016-04938. Y.W. is grateful for the partial support of the MIT J. S. Hennessy OGE Fellowship.

REFERENCES

BOUROUIBA, L., DEHANDSCHOEWERCKER, E. & BUSH, J. W. M. 2014 Violent expiratory events: on coughing and sneezing. *J. Fluid Mech.* **745**, 537–563.

CLANET, C. & LASHERAS, J. C. 1999 Transition from dripping to jetting. *J. Fluid Mech.* **383**, 307–326.

CLANET, C. & VILLERMAUX, E. 2002 Life of a smooth liquid sheet. *J. Fluid Mech.* **462**, 307–340.

CULICK, F. E. C. 1960 Comments on a Ruptured Soap Film. *J. Appl. Phys.* **31**, 1128–1129.

EGGERS, J. & DUPONT, T. F. 1994 Drop formation in a one-dimensional approximation of the Navier–Stokes equation. *J. Fluid Mech.* **262**, 205–221.

EGGERS, J., FONTELOS, M. A., JOSSERAND, C. & ZALESKI, S. 2010 Drop dynamics after impact on a solid wall: theory and simulations. *Phys. Fluids* **22**, 1–13.

FANTINI, E., TOGNOTTI, L. & TONAZZINI, A. 1990 Drop size distribution in sprays by image processing. *Comput. Chem. Engng* **14**, 1201–1211.

GILET, T. & BOUROUIBA, L. 2014 Rain-induced ejection of pathogens from leaves: revisiting the hypothesis of splash-on-film using high-speed visualization. *Integr. Compar. Biol.* **54**, 974–984.

GILET, T. & BOUROUIBA, L. 2015 Fluid fragmentation shapes rain-induced foliar disease transmission. *J. R. Soc. Interface* **12**, 20141092.

GORDILLO, J. M. & GEKLE, S. 2010 Generation and breakup of Worthington jets after cavity collapse. Part 2. Tip breakup of stretched jets. *J. Fluid Mech.* **663**, 331–346.

GORDILLO, J. M., LHUISSIER, H. & VILLERMAUX, E. 2014 On the cusps bordering liquid sheets. *J. Fluid Mech.* **754**, R1.

GORDILLO, J. M. & PEREZ-SBORID, M. 2005 Aerodynamic effects in the break-up of liquid jets: on the first wind-induced break-up regime. *J. Fluid Mech.* **541**, 1–20.

HOEPFFNER, J. & PARÉ, G. 2013 Recoil of a liquid filament: escape from pinch-off through creation of a vortex ring. *J. Fluid Mech.* **734**, 183–197.

JOSSERAND, C. & THORODDSEN, S. T. 2016 Drop impact on a solid surface. *Annu. Rev. Fluid Mech.* **48**, 365–391.

KELLER, J. B. 1983 Breaking of liquid films and threads. *Phys. Fluids* **26**, 3451–3453.
LASTAKOWSKI, H., BOYER, F., BIANCE, A. L., PIRAT, C. & YBERT, C. 2014 Bridging local to global dynamics of drop impact onto solid substrates. *J. Fluid Mech.* **747**, 103–118.
PETERS, I. R., VAN DER MEER, D. & GORDILLO, J. M. 2013 Splash wave and crown breakup after disc impact on a liquid surface. *J. Fluid Mech.* **724**, 553–580.
RAYLEIGH, LORD 1878 On the instability of jets. *Proc. R. Soc. Lond.* A **s1-10**, 4–13.
RIBOUX, G. & GORDILLO, J. M. 2015 The diameters and velocities of the droplets ejected after splashing. *J. Fluid Mech.* **772**, 630–648.
RIOBOO, R., MARENGO, M. & TROPEA, C. 2002 Time evolution of liquid drop impact onto solid, dry surfaces. *Exp. Fluids* **33**, 112–124.
ROISMAN, I. V., BERBEROVI, E. & TROPEA, C. 2009 Inertia dominated drop collisions. I. On the universal flow in the lamella. *Phys. Fluids* **21**, 052103.
ROZHKOV, A., PRUNET-FOCH, B. & VIGNES-ADLER, M. 2002 Impact of water drops on small targets. *Phys. Fluids* **14**, 3485–3501.
ROZHKOV, A., PRUNET-FOCH, B. & VIGNES-ADLER, M. 2004 Dynamics of a liquid lamella resulting from the impact of a water drop on a small target. *Proc. R. Soc. Lond.* A **460**, 2681–2704.
SAVART, F. 1833*a* Me?moire sur le choc dune veine liquide lance?e sur un plan circulaire. *Ann. Chim.* **54**, 56–87.
SAVART, F. 1833*b* Suite du me?moire sur le choc dune veine liquide lance?e sur un plan circulaire. *Ann. Chim.* **54**, 113–145.
SAVVA, N. & BUSH, J. W. M. 2009 Viscous sheet retraction. *J. Fluid Mech.* **626**, 211–240.
SCHARFMAN, B. E., TECHET, A. H., BUSH, J. W. M. & BOUROUIBA, L. 2016 Visualization of sneeze ejecta: steps of fluid fragmentation leading to respiratory droplets. *Exp. Fluids* **57**, 24.
SCHULKES, R. M. S. M. 1996 The contraction of liquid filaments. *J. Fluid Mech.* **309**, 277–300.
STERLING, A. M. & SLEICHER, C. A. 1975 The instability of capillary jets. *J. Fluid Mech.* **68**, 477–495.
THORODDSEN, S. T., TAKEHARA, K. & ETOH, T. G. 2012 Micro-splashing by drop impacts. *J. Fluid Mech.* **706**, 560–570.
TING, L. & KELLER, J. B. 1990 Slender jets and thin sheets with surface tension. *SIAM J. Appl. Math.* **50** (6), 1533–1546.
VILLERMAUX, E. 2007 Fragmentation. *Annu. Rev. Fluid Mech.* **39**, 419–446.
VILLERMAUX, E. & BOSSA, B. 2011 Drop fragmentation on impact. *J. Fluid Mech.* **668**, 412–435.
VILLERMAUX, E., MARMOTTANT, PH. & DUPLAT, J. 2004 Ligament-mediated spray formation. *Phys. Rev. Lett.* **92**, 074501.
WANG, Y. & BOUROUIBA, L. 2017 Drop impact on small surfaces: thickness and velocity profiles of the expanding sheet in the air. *J. Fluid Mech.* **814**, 510–534.
WANG, Y. & BOUROUIBA, L. 2018 Non-isolated drop impact on surfaces. *J. Fluid Mech.* **835**, 24–44.
YARIN, A. L. 2006 Drop impact dynamics: splashing, spreading, receding, bouncing. . . . *Annu. Rev. Fluid Mech.* **38**, 159–192.
YARIN, A. L. & WEISS, D. A. 1995 Impact of drops on solid surfaces: self-similar capillary waves, and splashing as a new type of kinematic discontinuity. *J. Fluid Mech.* **283**, 141–173.